On the magnetic nanoparticle injection strategy for hyperthermia treatment

Jiang, Qian; Ren, Feng; Wang, Chenglei; Wang, Zhaokun; Kefayati, Gholamreza; Kenjeres, Sasa; Vafai, Kambiz; Liu, Yang; Tang, Hui

DOI
10.1016/j.ijmecsci.2022.107707

Publication date
2022

Document Version
Final published version

Published in
International Journal of Mechanical Sciences

International Journal of Mechanical Sciences 235 (2022) 107707

Contents lists available at ScienceDirect

International Journal of Mechanical Sciences

journal homepage: www.elsevier.com/locate/ijmecsci

On the magnetic nanoparticle injection strategy for hyperthermia treatment

Qian Jiang [a], Feng Ren [a,b], Chenglei Wang [a], Zhaokun Wang [a], Gholamreza Kefayati [c], Sasa Kenjeres [d,e], Kambiz Vafai [f], Yang Liu [a], Hui Tang [a,*]

[a] Department of Mechanical Engineering, The Hong Kong Polytechnic University, Hong Kong,China
[b] School of Marine Science and Technology, Northwestern Polytechnical University, Xi'an, Shaanxi 710072, China
[c] School of Engineering, University of Tasmania, Hobart 7001, Tasmania, Australia
[d] Transport Phenomena Section, Department of Chemical Engineering, Faculty of Applied Sciences, The Netherlands
[e] J. M. Burgers Center for Fluid Mechanics, Delft University of Technology, Van der Maasweg 9, Delft 2629, HZ, The Netherlands
[f] Mechanical Engineering Department, University of California, Riverside, CA 92521, USA

ARTICLE INFO

Keywords:
Magnetic hyperthermia treatment
Magnetic nanoparticle
Lattice Boltzmann method
Particle swarm optimization

ABSTRACT

We developed a dedicated computational framework by coupling the lattice-Boltzmann-method (LBM) modeling and the particle-swarm-optimization (PSO) algorithm to search optimal strategies of magnetic nanoparticle (MNP) injection for hyperthermia-based cancer treatment. Two simplified tumor models were considered: a circular model representing geometrically regular tumors and an elliptic model representing geometrically irregular tumors, both sharing the same area. The temperature distribution in the tumor and its surrounding healthy tissue was predicted by solving the Pennes' bio-heat transfer equation (PBHTE). Both single- and multi-site injection strategies were explored. The results suggest that the multi-site injection strategies generally work well, while the single-site injection strategy fails even on the simplest circular tumor model. The more the injection sites, the better the performance. In particular, when the number of injection sites reaches eight, all temperature requirements can be nearly 100% satisfied in both tumor models. Whether or not including the minimum dose requirement in the objective function only affects the optimization results by less than 2%. The thermal dose was also assessed by considering both temperature and heat exposure time. It was found that the optimal multi-site injection strategies perform reasonably well for both tumor models. Although the setting is only two dimensional and the optimization is on very simplified tumor models, the framework adopted in this present study works well and can provide useful insights into magnetic hyperthermia treatment.

1. Introduction

Hyperthermia treatment, or thermotherapy, is a cancer therapeutic procedure in which tumor tissues are locally heated to approximately above 43 °C, thereby to ablate malignant cells without overheating the surrounding healthy tissue [1–3]. The damage on cells is irreversible since high temperature will cause the protein denaturation [4]. As one of hyperthermia modalities, magnetic hyperthermia treatment utilizes magnetic nanoparticles (MNPs), which are injected into tumor tissues and subjected to an alternating magnetic field (AMF), to generate the required heat at target regions [5–7]. Such a heat generation mechanism offers magnetic hyperthermia treatment several advantages over conventional approaches, such as more targeted and homogeneous heating, harmless to human body, and more effective treatment [8–10]. Although having been demonstrated to be effective, magnetic hyperthermia treatment is still facing a great challenge, i.e., how to impose fatal thermal damage to cancerous tissues, while minimizing the damage to surrounding healthy tissues? To tackle this challenge, optimal MNP concentrations and spatial distributions must be identified, which requires detailed heat and mass transfer analysis.

For the MNPs used in magnetic hyperthermia treatment, magnetite (Fe_3O_4) has been chosen in many studies as an ideal candidate, since such iron-oxide nanoparticles bear favorable magnetic properties and low toxicity [11–13]. Nevertheless, iron-based nanoparticles are still genotoxic to healthy skin and lung tissue [14]. According to Karponis et al. [11], iron intake in human body should be moderate, and overdose may shorten life expectancy.

Regarding the distribution of MNPs, Liangruksa et al. [15] numerically compared the performance of uniform, exponential and Gaussian distributions, and concluded that the Gaussian distribution can provide the best efficacy while minimizing the possibility of generating hot spots in the tumor. Salloum et al. [16] also confirmed that the Gaussian distribution is a good fit with the observation from MNP delivery experiments, which agrees with the analytical diffusion prediction. It

* Corresponding author.
E-mail address: h.tang@polyu.edu.hk (H. Tang).

https://doi.org/10.1016/j.ijmecsci.2022.107707
Received 1 April 2022; Received in revised form 24 August 2022; Accepted 29 August 2022
Available online 6 September 2022

Nomenclature

Parameters

(x, y)	Coordinates of injection site, m
α	Reference thermal diffusivity, m^2/s
β	Inclination angle, °
β_0	Reference inclination angle, °
χ_0	Equilibrium susceptibility
$\dot{m}$	density flux, kg/m^3-s
$\mathbf{\Psi}$	Source term vector in LBM
$\mathbf{g}$	Five-dimensional distribution function vector in LBM
$\omega_1 \sim \omega_4$	Weighting factors of each basic requirement in objective function
$\boldsymbol{\Phi}$	Volume fraction with time variant
ϕ	Volume fraction without time variant
ϕ_0	Reference volume fraction
ρ	Density, kg/m^3
σ	Standard deviation, m
σ_0	Reference standard deviation, m
τ_B	Brownian relaxation time, s
τ_N	Neel relaxation time, s
τ_R	Effective relaxation time, s
c	Specific heat, J/(kg-K)
C_{EM}	Coefficient, a function of temperature
$CEM43$	Cumulative equivalent time at 43°C, min
D	Mass diffusivity, m^2/s
d	distance of injection site, m
d_0	Reference distance
d_{tum}	Diameter of circular tumor, m
Err	Error percentage, %
$f(x)$	Test function for PSO
J	Objection function
k	Thermal conductivity, W/m-K
k_β	Inclination angle ratio
k_ϕ	Volume fraction ratio
k_σ	Standard deviation ratio
k_d	Distance ratio of injection site
L	Length of healthy tissue, m
l	Number of time intervals
$N_x \times N_y$	Grid number in LBM
Q	Heat induced by MNPs, W/m^3
R_{CEM43}	Percentage ratio of area for $CEM43 \geq 60$ min
R_{int}	Temperature requirement at interface between healthy tissue and tumor tissue
R_{tis}	Temperature requirement in healthy tissue
R_{tum}	Temperature requirement in tumor tissue
S	Area, m^2
T	Temperature, °C
t	Time, min
V	Volume of injected MNP solution, m^3
V_H	Hydrodynamic volume of single MNP, m^3
V_M	Magnetic volume of single MNP, m^3

Subscripts

b	Blood
c	Tumor center
i	Injection site number
mnp	Magnetic nanoparticles
nf	Nanofluid, the mixture of tissue and injected MNPs
opt	Optimal value
r	The rightmost point on tumor boundary
tis	Healthy tissue
tum	Tumor tissue

was believed that, since the MNP injection rate and the blood infusion rate are slow enough, achieving the Gaussian distribution for MNPs in real situations is feasible [16,17].

In practice, it is challenging to manually fabricate the MNP distribution for expected heating results, which is especially true for tumors with irregular shapes. Golneshan and Lahonian [18] simulated the MNP diffusion in a tumor with complex geometry, and pointed out that with the same diffusion time multi-site injection is able to create more uniform distribution and covers a larger area than single-site injection. Other studies also demonstrated that multi-site injection is a good strategy that can help enhance the effectiveness of magnetic hyperthermia treatment [19,20].

Note that, in the above multi-site injection studies, the injection sites were arbitrarily selected. To explore the best injection sites, using optimization algorithms may be of great help. So far only a limited number of studies were reported in this aspect though. For example, Salloum et al. [21] and Tang et al. [22] applied the Nelder–Mead simplex method, and Barba et al. [23] applied the epsilon-constraint approach to optimize the temperature distribution in a tumor. However, both these two methods are local optimization algorithms, bearing the drawbacks of only finding local optima and relying very much on the initial guess of parameters, and hence are not capable of solving discrete optimization problems [24]. To address this issue, in a simple setting without considering the influence of injection number and geometrical complexity, Tang et al. [25] compared two stochastic optimization techniques, i.e., the simulated annealing (SA) and the particle swarm optimization (PSO), in exploring the best temperature distribution for hyperthermia treatment, and illustrated that the PSO shows better ability in handling a large number of independent variables. Nevertheless, with a two-site injection strategy they still had a 19.6% injury rate in healthy tissue when achieving a 99.9% ablation rate in tumor. A similar treatment efficacy was also reported by Barba et al. [26], who applied the non-dominated sorting genetic algorithm (NSGA) on two-site injections and achieved a 91.2% ablation rate in tumor along with a 16.7% injury rate in healthy tissue.

To further enhance the treatment efficacy, in this study we aim to explore optimal MNP injection strategies for magnetic hyperthermia. To facilitate effective and efficient search, a dedicated computational framework is developed, in which the heat generation and transfer in tissues is simulated by solving the Pennes' bioheat transfer equation (PBHTE) using the lattice Boltzmann method (LBM), and the MNP injection strategies are evaluated and optimized using the PSO algorithm. This "modeling + optimization" framework is then demonstrated on two selected tumor models: one is a circle representing a geometrically regular tumor, and the other is an ellipse representing a geometrically irregular tumor. Both single- and multi-site injection strategies are evaluated. The effects of some key factors, such as the minimum dose requirement, are also studied. Moreover, the thermal dose in the optimal multi-site injection strategies is assessed by considering both temperature and heat exposure time.

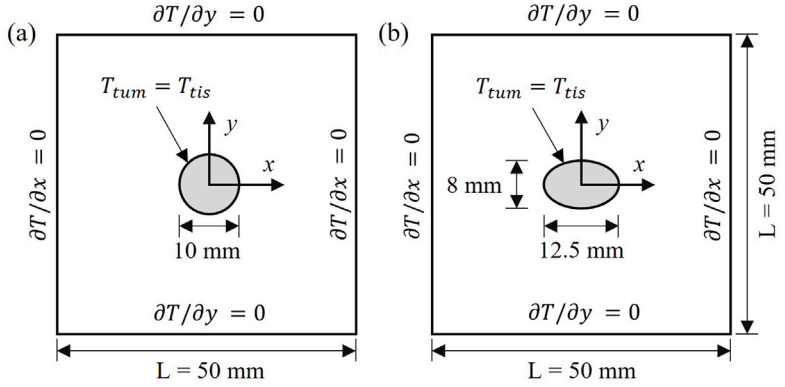

Fig. 1. Schematics of two tumor models surrounded by healthy tissue: (a) a circular tumor model, and (b) an elliptical tumor model. The gray regions represent the tumor and the outer white regions represent the healthy tissue.

2. Problem description and methodology

The relevant physical and mathematical models will be introduced in this section. First, the two selected tumor models are described in Section 2.1. Then, the governing equations for simulating MNP-induced heat generation and transfer in tissues are introduced in Section 2.2. Last, the optimization algorithm adopted in the present study is presented in Section 2.3.

2.1. Problem description

Two simplified tumor models were chosen in the present study, as sketched in Fig. 1. One is a circle representing a geometrically regular tumor, and the other is an ellipse representing a geometrically irregular tumor. The diameter of the circular tumor is set as 10 mm. The major and minor axes of the elliptical tumor are set as 12.5 mm and 8 mm, respectively. Hence both tumors have the same area. Surrounded by healthy tissue, each tumor is located at the center of a selected 50 mm × 50 mm tissue block. Assuming the adiabatic condition on the outside boundaries of the tissue block, the hyperthermia treatment is realized through heat generation by the AMF driven MNPs, which are injected at chosen sites in the tumor. Meanwhile, heat will also be taken away by the blood flow embedded in the tumor and the tissue.

2.2. Governing equations

The temperature distribution in the tumor and its surrounding healthy tissue, T, is evaluated using the Pennes' bioheat transfer equation (PBHTE) [27], which has been widely adopted for predicting magnetic hyperthermia treatment efficacy [28–30]. It relates the evolution of temperature in tissue with physiological and environmental factors, such as the blood perfusion and MNP-generated heat

$$(\rho c)_{nf}\frac{\partial T}{\partial t} = k_{nf}\left(\frac{\partial^2 T}{\partial^2 x}+\frac{\partial^2 T}{\partial^2 y}\right)+\dot{m}_b c_b(T_b-T)+Q \tag{1}$$

where ρ, c and k are density, specific heat and thermal conductivity, respectively. The subscript "nf" denotes properties of nanofluid or modified tissue that is a mixture combining the tissue and the injected MNPs, and "b" denotes properties of blood. The properties of nanofluid can be determined for given MNP's volume fraction ϕ [31–33]

$$(\rho c)_{nf} = \phi(\rho c)_{mnp}+(1-\phi)(\rho c)_{tis} \tag{2a}$$

$$k_{nf} = k_{tis}\frac{k_{mnp}+2k_{tis}-2\phi(k_{tis}-k_{mnp})}{k_{mnp}+2k_{tis}+\phi(k_{tis}-k_{mnp})} \tag{2b}$$

Note that the subscript "tis" here includes the healthy tissue and the tumor tissue, both sharing the same properties for simplification since the difference in their thermal properties is only up to about 5% [34–36]. The detailed properties for the nanofluid formation are listed in Table 1.

Table 1
Properties of the tissue and nanoparticles [34,37,38].

Tissue properties	Value	MNP properties	Value
ρ_{tis} (kg/m^3)	1052	ρ_{mnp} (kg/m^3)	5200
c_{tis} (J/kg-K)	3800	c_{mnp} (J/kg-K)	670
k_{tis} (W/m-K)	0.5	k_{mnp} (W/m-K)	6

The second term on the right hand side of Eq. (1), $\dot{m}_b c_b(T_b - T)$, describes the rate of heat transfer from blood to tissue, where T_b = 37 °C is the normal temperature of blood and $\dot{m}_b$ is the mass flow rate of perfusing blood per unit volume. According to Lang et al. [39], $\dot{m}_b$ depends on local temperature as follows

In healthy tissue:

$$\dot{m}_b = \begin{cases} 0.45+3.55\exp[-(T-45)^2/12] & T\le 45°\text{C} \\ 4.0 & T>45°\text{C}\end{cases} \tag{3}$$

In tumor:

$$\dot{m}_b = \begin{cases} 0.833 & T<37°\text{C} \\ 0.8333-(T-37)^{4.8}/5438.0 & 37<T\le 42°\text{C} \\ 0.416 & T>42°\text{C}\end{cases} \tag{4}$$

The last term in Eq. (1), Q, represents the heat released from MNPs as induced by an external AMF. Its evaluation is provided in Appendix A.

Once injected at a selected site (x_i, y_i), the evolution of MNPs' volume fraction can be determined analytically as two-dimensional diffusion

$$\Phi_i(x,y,t) = \frac{V_i}{4\pi Dt}\exp\left[-\frac{(x-x_i)^2+(y-y_i)^2}{4Dt}\right] \tag{5}$$

where D is the mass diffusivity and V_i is the volume of injected MNP solution. Eq. (5) clearly indicates that, at any instant, the spatial distribution of MNPs follows the Gaussian distribution with the variance $2Dt$.

Note that, in magnetic hyperthermia treatment the AMF is usually not applied at the time of injection. Instead, it is applied after the MNPs have sufficiently diffused in the tumor. Since the MNP diffusion is usually much slower than the thermal diffusion, which is reflected by the large Lewis number $Le = \alpha/D = 125$ (α is the thermal diffusivity) used in the present study, the temperature field governed by Eq. (1) is solved by "freezing" the time for the mass diffusion [40]. That is, we only consider a temperature diffusion problem by replacing $2Dt$ with a constant variance σ^2, modifying Eq. (5) into

$$\phi_i(x,y) = \frac{V_i}{2\pi\sigma^2}\exp\left[-\frac{(x-x_i)^2+(y-y_i)^2}{2\sigma^2}\right] \tag{6}$$

In the scenario of multi-site injections, we assume all injections are conducted at the same time and with the same dose, hence having the same MNP distribution. The total volume fraction at a given location (x, y) is then the superposition of all injections

$$\phi(x,y) = \sum_{i=1}^{n} \phi_i(x,y) \tag{7}$$

where n is the number of injections.

The temperature field governed by Eq. (1) is solved using a lattice Boltzmann method (LBM) based computational framework. This mesoscopic approach is an alternative to conventional finite-difference, finite-element or finite-volume methods for computational fluid dynamics (CFD), with its distinctive merits of easy programming, manageable computer resources and numerical stability and accuracy [41]. Refer to Appendix B for the formulation and validation of this computational framework.

2.3. Optimization

The steady-state temperature distribution obtained from solving Eq. (1) is then used to evaluate the performance of magnetic hyperthermia treatment and facilitate the optimization. For the optimization, the parameters to be controlled in this study include the number of injection sites n, the location of injections (x_i, y_i), the dose applied in each injection V_i, and the variance of MNP distribution σ^2 that reflects the timing of applying the AMF.

To enable efficient and effective searches, some of the above parameters are normalized. That is, the location of injections is measured by a distance ratio $k_{d,i} = d_i/d_0$ where $d_i = \sqrt{x_i^2 + y_i^2}$ is the distance of the injection site from the tumor center and d_0 is a chosen reference distance from the tumor center to point (x_0, y_0). The spatial distribution of MNPs is measured by a standard deviation ratio $k_\sigma = \sigma/\sigma_0$ where σ_0 is a reference standard deviation obtained 20 min after the MNP injection. The dose of each injection can also be measured by a dose ratio in a similar way. However, here we replace V_i by another quantity related to the volume fraction, k_ϕ, through $V_i = k_\sigma^2 k_\phi \phi_0$, where ϕ_0 is a reference volume fraction, so that only one optimization parameter appears in the coefficient of the exponential function. As such, Eq. (6) can be re-written as

$$\phi_i(x,y) = \frac{k_\phi \phi_0}{2\pi\sigma_0^2} \exp\left[-\frac{(x - k_{d,i}x_0)^2 + (y - k_{d,i}y_0)^2}{2k_\sigma^2\sigma_0^2}\right] \tag{8}$$

Note that k_ϕ and k_σ do not carry the subscript i since we have assumed all injections share the same MNP dose and distribution.

In hyperthermia treatment, it is expected that the cancer tissue can be ablated at a temperature above a threshold, i.e., 43 °C, while the healthy tissue stays safe by strictly keeping its temperature under this threshold. According to Hervault and Thanh [42], the temperature in both types of tissues should also be maintained under 46 °C to avoid possible inflammatory responses. Moreover, overdose of iron-based MNPs may shorten life expectancy [11], so it is necessary to maintain a low level of injection quantity. Therefore, four basic requirements are formulated to evaluate the performance of magnetic hyperthermia treatment simulated in the present study, i.e.,

$$R_{tum} = \frac{S_{43°C \le T < 46°C \text{ in tumor}}}{S_{tumor}} \tag{9a}$$

$$R_{tis} = \frac{S_{T<43°C \text{ in healthy tissue}}}{S_{healthy\ tissue}} \tag{9b}$$

$$R_{int} = \exp\left(-\sqrt{\frac{1}{N}\sum_{i=1}^{N}(T_i - 43)^2}\right) \tag{9c}$$

$$R_{dose} = 1 - \sqrt[3]{nk_\phi k_\sigma^2} \tag{9d}$$

where S represents area and N is the total number of points sampled along the tumor–healthy-tissue interface. R_{tum} defines a ratio of the tumor area with temperature between 43 °C and 46 °C to the entire tumor area, which evaluates how much the temperature distribution in the tumor satisfies the requirement. Similarly, R_{tis} defines a ratio of the area in the healthy tissue with temperature below 43 °C over the entire healthy tissue area, evaluating how much the temperature distribution in the healthy tissue satisfies the requirement. R_{int} describes how different the temperature at the tumor–healthy-tissue interface deviates from the required 43 °C. Different from the above three temperature requirements, R_{dose} evaluates the dose requirement, since the total volume of the dose is proportional to $nk_\phi k_\sigma^2$. Note that, to improve the optimization efficiency, the ideal maximum of all the four requirement variables are designed to be 1, the larger the better.

With the four requirement variables defined, an objective function for optimization can be formulated as

$$J = \omega_1 R_{tum} + \omega_2 R_{tis} + \omega_3 R_{int} + \omega_4 R_{dose} \tag{10}$$

To ensure J roughly varies between 0 and 1 for good optimization performance, and to put more emphasis on the temperature distributions, the weighting factors ω_1, ω_2, ω_3, ω_4 are set as 0.3, 0.3, 0.2, 0.2, respectively, after several trial runs.

The optimization is conducted to search the maximum J using the particle swarm optimization (PSO) method, so that the best MNP distribution for magnetic hyperthermia treatment can be identified. PSO is a heuristic optimization algorithm, which performs stochastic search, makes few or no assumptions about the problem being optimized and can search very large spaces of candidate solutions [43]. See Appendix C for more details about this optimization method.

The optimization will generate a set of optimal ratios, i.e., k_ϕ, k_σ and k_d, with which the best waiting time t_{opt}, the best volume of MNPs V_{opt} and the best distance of injection sites from the tumor center d_{opt} can be determined as

$$t_{opt} = \frac{k_\sigma^2\sigma_0^2}{2D} \tag{11a}$$

$$V_{opt} = nk_\sigma^2 k_\phi \phi_0 \tag{11b}$$

$$d_{opt} = k_d d_0 \tag{11c}$$

3. Results and discussion

This section presents the optimization results and related discussions about hyperthermia treatment on the two selected tumor models under different MNP injection strategies. Sections 3.1 and 3.2 mainly focus on the optimized temperature distributions, whereas Section 3.3 further considers the time of exposure to heat in the optimization.

3.1. Circular tumor

For this geometrically regular tumor, we assume all MNP injections, if more than one, share the same dose and occur at the same time. In addition, all injection sites share the same distance from the center of the tumor and are evenly distributed in the azimuthal direction. As such, only the three ratios introduced in Section 2.3, i.e., k_ϕ, k_σ and k_d, are involved in the optimization. Their corresponding reference values are chosen as follows: $\phi_0 = 1.25$ mm^2 to ensure the volume fraction of MNPs is not too large, $\sigma_0 = 1.55$ mm is the standard deviation of the MNP distribution 20 minutes after the injection, which is obtained by solving Eq. (5), and $d_0 = 4.5$ mm is 90% the tumor radius that defines the allowed area for MNP injections.

Three injection cases are considered here, namely one-site, four-site and eight-site injections. For the one-site injection, it has to be at the tumor center due to the geometrical symmetry, and hence $k_d = 0$. For the other two cases, one injection is located along the x axis, while the others are evenly distributed in the azimuthal direction.

In each PSO search, 20 particles are adopted and evolve for 300 generations. Take the four-site injection case as an example, the PSO

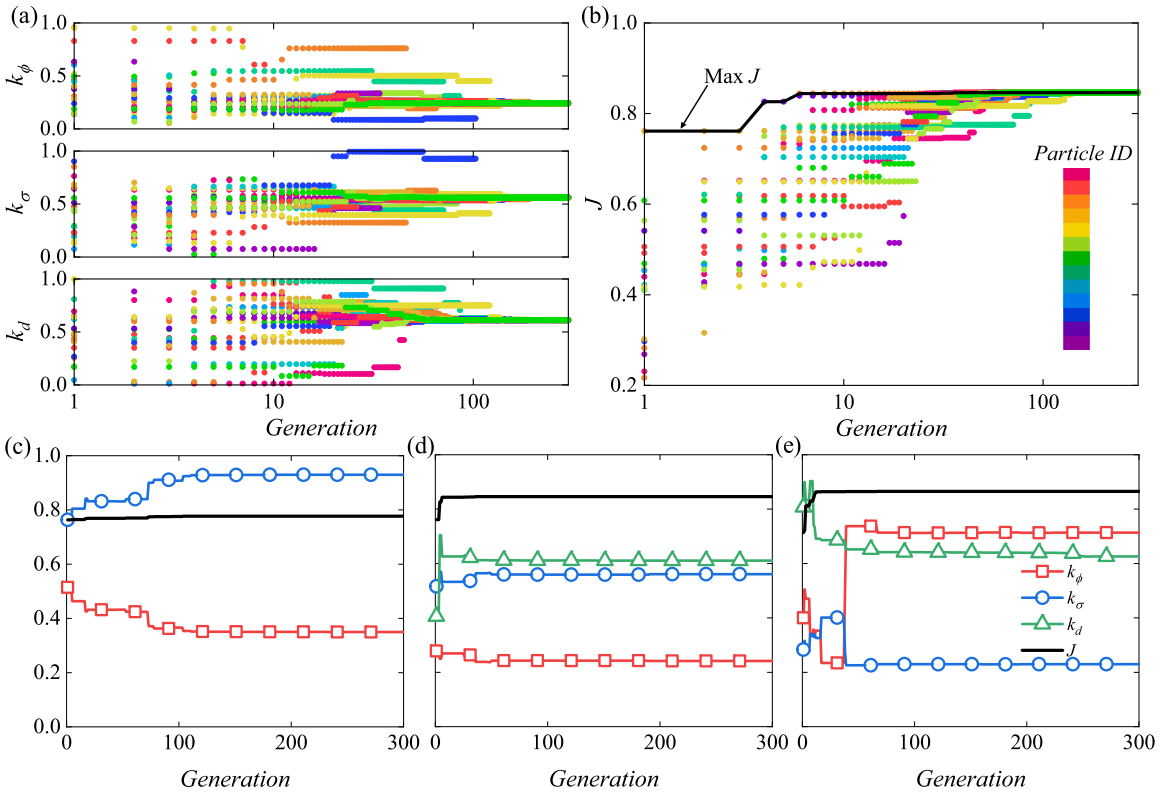

Fig. 2. PSO searching process on the circular tumor model: Evolution of (a) the three ratios, i.e., k_ϕ, k_σ and k_d, and (b) the objective function J in the four-site injection case; Evolution of optimal parameters and corresponding J in the cases of (c) one-site injection, (d) four-site injection, and (e) eight-site injection. The black lines depict the envelope of the maximum J.

searching process is shown in Fig. 2(a) and (b). Initially, the three optimization parameters for all particles in the swarm are randomly assigned between 0 and 1. After several generations, some particles gradually identify suitable parameter combinations for increasing the objective function J, and pass the experience to other particles. This effective learning process makes the three parameters of all particles converge to their respective optimal values after about 100 generations, and results in a consistent rise in the maximum J of each generation until it levels off at its optimal value (See Fig. 2(b)).

Figs. 2(c) to (e) show the evolution of the optimization parameters and the collectively produced maximum J in the three injection cases. It reveals that all the three cases can quickly find their optima, reflecting the appropriateness of the adopted PSO settings. Specifically, the four-site injection case finds its optimal parameter combination with the fastest pace, roughly after 50 generations, while the one-site and eight-site injection cases take a bit longer, roughly after 100 and 75 generations, respectively. It is seen that, with the increase of injection number, the optimal k_σ monotonically reduces from 0.93 to 0.23, which, according to Eq. (11a), reflects that the optimal waiting time for the AMF significantly decreases, from 17.3 minutes for one-site injection, to 6.3 minutes for four-site injection, and then to 1.1 minutes for eight-site injection. It also shows that the optimal k_d is about 0.62 in the two multi-site injection cases, which, according to Eq. (11c), indicates that the optimal location of the injection sites is about 56% the tumor radius from the center. The most important observation made from these optimizations is that multi-site injections are beneficial to hyperthermia treatment, as confirmed by the best performance achieved in the eight-site injection case (with the largest $J = 0.87$) and the worst performance achieved in the single-site injection case (with the lowest $J = 0.78$).

Table 2 also lists the values at the optimal conditions for the four requirements and the corresponding physical quantities as defined in Eq. (11). It is noticed that R_{tum}, the ratio of the tumor area satisfying the hyperthermia temperature requirement, is only 0.708 for the single-site injection case. Compared to those values almost or perfectly 1 in the multi-site injection cases, it clearly indicates that the single-site injection fails to fulfill the temperature requirements. Indeed, in this case a large portion at the tumor center is overheated (i.e., $T > 46$ °C), as revealed in the temperature contour shown in Fig. 3(d). On the contrary, the two multi-site injection cases can generally fulfill all the three temperature requirements, i.e., R_{tum}, R_{tis} and R_{int}. The effectiveness of multi-injection strategy has also been reported by Singh et al. [19]. If comparing the temperature distribution along the interface, however, the eight-site injection case slightly outperforms the four-site injection case, which is evidenced by the listed R_{int} values in Table 2 and the radial temperature distribution near the interface as shown in the inset of Fig. 3(g). It is this slight advantage that leads to a higher J for the eight-site injection case.

From Table 2, it is also found that the optimal total dose for MNP injections varies slightly (less than 1%) among the three cases, suggesting that the optimization may not be sensitive to the dose requirement R_{dose}, i.e., Eq. (9d). To further confirm this, we conduct another optimization study, in which R_{dose} is not included in the objective function. As revealed in Table 3, although including R_{dose} in the objective function does help reduce the total dose, the reduction is very marginal, which does not really affect the optimization results.

From Fig. 3(e), one can see that the multi-site injection may result in directional difference in the temperature distribution, which then leads to nonuniform temperature distribution along the circular interface, as indicated in Table 2. This directional difference can be mitigated by adding more injection sites along the azimuthal direction, like in the eight-site injection case as shown in Fig. 3(f). Since in this study the chosen computational domain is in a square shape, the direction of the four-site injections could affect the optimization results. To assess this effect, another four-site injection case is simulated, where the original four injection sites are relocated from the 0° (i.e., x) and 90°

Table 2
Optimization results for the one-, four- and eight-site injection cases on the circular tumor model.

Injection strategy	R_{tum}	R_{tis}	R_{int}	R_{dose}	J	t_{opt}, min	V_{opt}, mm^2	d_{opt}, mm
One-site	0.708	0.999	0.994	0.329	0.78	17.3	0.378	0
Four-site	0.987	0.999	0.925	0.328	0.85	6.3	0.380	2.75
Eight-site	1.000	0.999	0.998	0.330	0.87	1.1	0.376	2.82

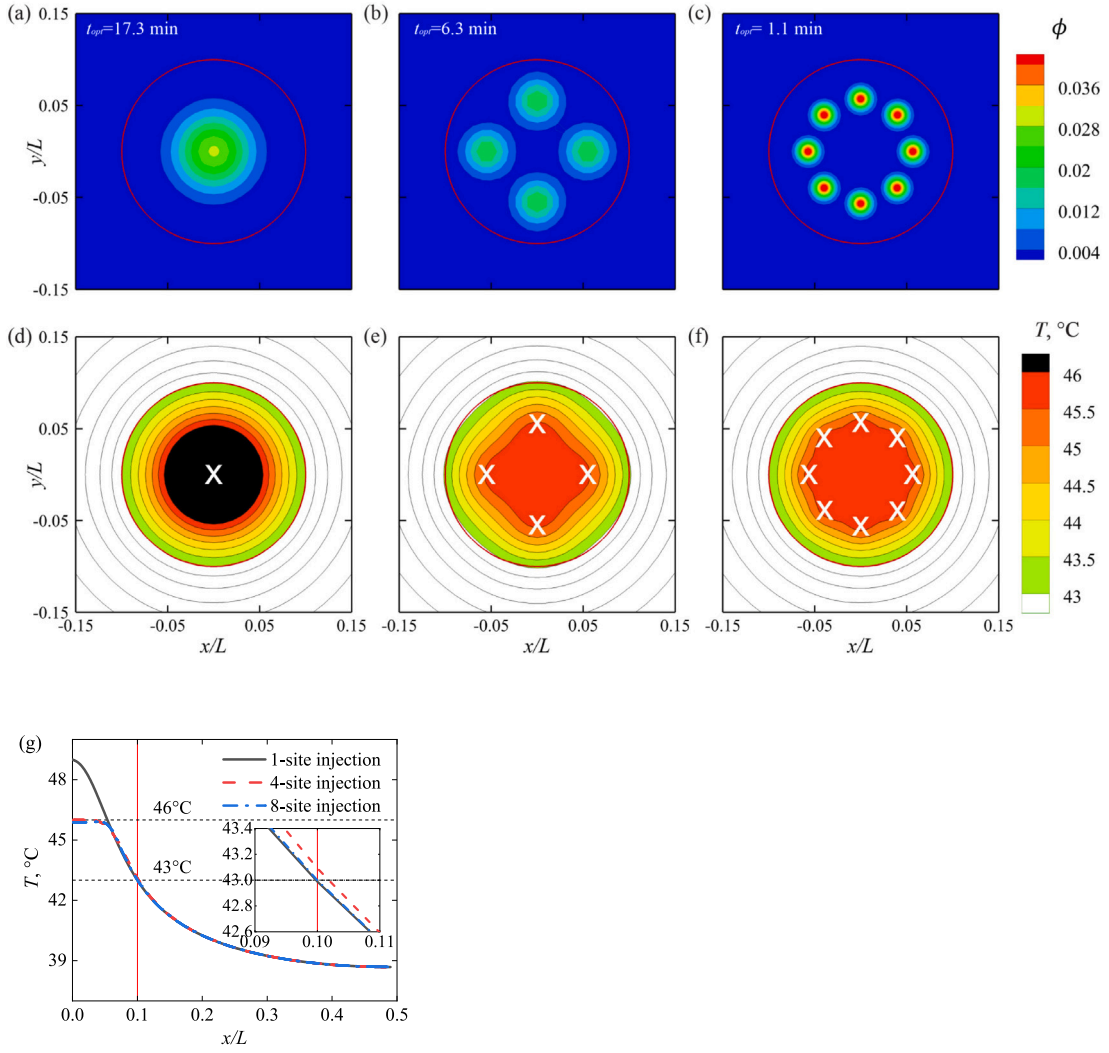

Fig. 3. Optimal concentration and temperature distributions on the circular tumor model: (a), (b) and (c) the concentration fields for one-, four- and eight-site injection cases, respectively; (d), (e) and (f) the corresponding temperature fields. The white crosses denote MNP injection sites. The red circle represents tumor boundary. In the temperature fields, the black color denotes regions with temperature above 46 °C, the white color denotes regions with temperature under 43 °C, and the other colors denote regions with temperature ranging between 43 °C and 46 °C. (g) the optimal temperature distribution along the x axis. The inset shows more details near the tumor boundary, i.e., $x/L = 0.1$ as represented by the vertical red line.

Table 3
Comparison of optimization results between cases including and not including the minimum dose requirement.

Injection strategy		R_{tum}	R_{tis}	R_{int}	V_{dose}, mm^2
One-site	w R_{dose}	0.708	0.999	0.994	0.378
	w/o R_{dose}	0.708	0.999	0.994	0.378
Four-site	w R_{dose}	0.987	0.999	0.925	0.379
	w/o R_{dose}	1.000	0.999	0.936	0.384
Eight-site	w R_{dose}	1.000	0.999	0.998	0.376
	w/o R_{dose}	1.000	0.999	0.998	0.377

(i.e., y) axes to the ±45° axes. The new optimization results reveal that such a rotation does not really affect the optimal distributions of MNPs and temperature, as shown in Fig. 4. Meanwhile, although not listed here for brevity, the rotation has negligible effects on the hyperthermia treatment performance in terms of the temperature and dose requirements.

3.2. Elliptical tumor

In general, tumors do not grow isotropically to form an ideal circle. Instead, they often appear in irregular shapes. To tackle the complexity caused by the geometric irregularity, another set optimization studies is conducted on an elliptical tumor. As sketched in Fig. 1(b), this tumor has a 12.5 mm major axis and a 8 mm minor axis, hence sharing the same area with the circular tumor studied in Section 3.1.

Four different injection cases are considered for this elliptical tumor, namely one-site, two-site, four-site and eight-site injections. The new

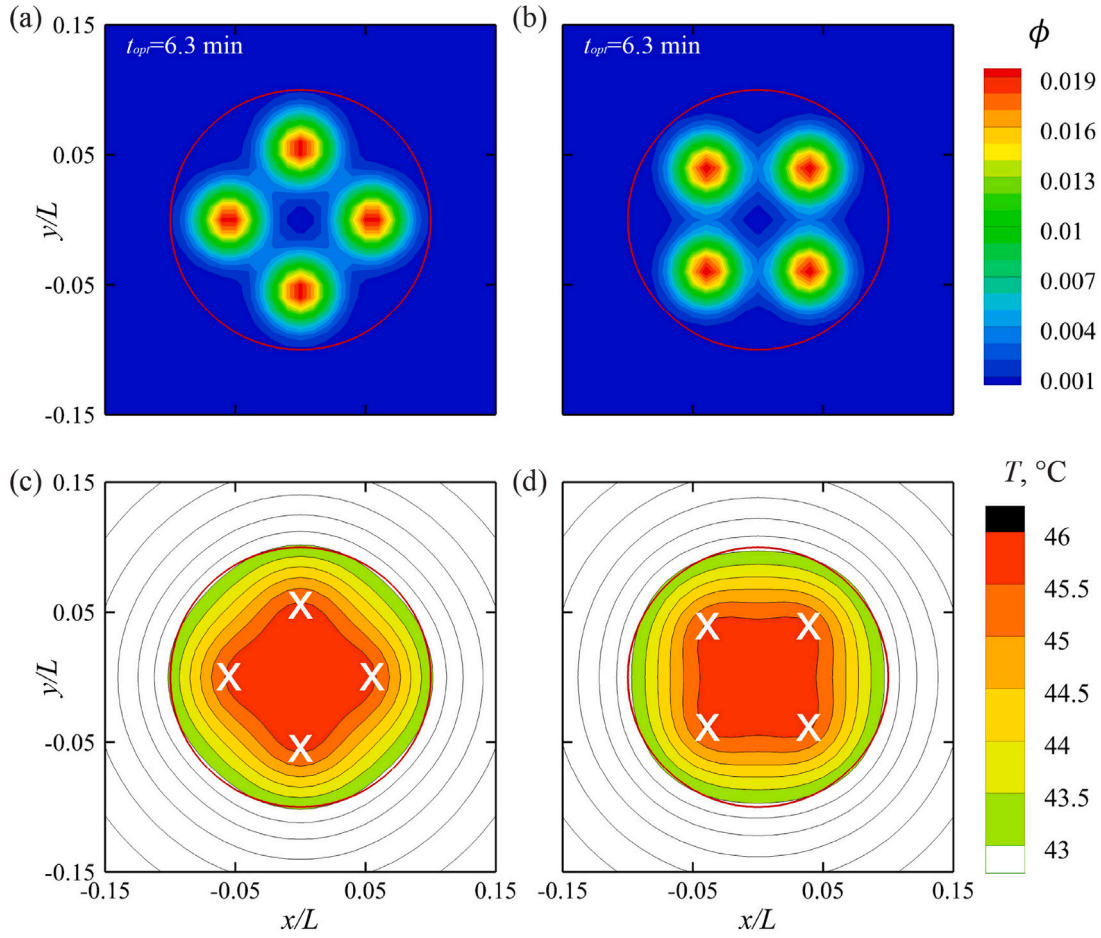

Fig. 4. Optimal concentration and temperature distributions in two different four-site injection cases on the circular tumor model. In (a) and (c) the four injection cites are arranged along x and y axes, which are rotated for 45° in (b) and (d). The red circle represents tumor boundary. The white crosses denote the injection sites. In the temperature fields, the white color denotes regions with temperature under 43 °C, and the other colors denote regions with temperature ranging between 43 °C and 46 °C.

two-site injection case is introduced to represent the simplest injection pattern in order to address the geometric irregularity, where the injection sites are arranged along the major axis, symmetric about the tumor center. In the four-site injection case, two injection sites are symmetrically arranged along the major axis, while the other two are symmetrically arranged along the minor axis. For the eight-site injection case, four more sites are introduced, which are arranged along two lines that deviate from the major axis with an inclination angle β, as denoted in Fig. 6(d).

To deal with the geometric irregularity, in the optimization the injection sites are allowed to vary independently along different axes. This is different from the cases for the circular tumor, where the distances of the injection sites from the tumor center along different axes are set identical. As such, the original location ratio parameter for the circular tumor, k_d, becomes k_{dh} along the major (horizontal) axis, k_{dv} along the minor (vertical) axis, and k_{di} along the inclined axes, wherever applicable, for the elliptical tumor. The corresponding ranges are set as $d_{h0} = 1.25d_0$, $d_{v0} = 0.8d_0$, and $d_{i0} = d_0$, respectively, according to the given shape of the elliptical tumor. For the eight-site injection case, the angle of the inclined axes is also allowed to vary through a new ratio parameter k_β together with a preset range $\beta_0 = 90°$. The arrangements for these distance parameters are also listed in Table 4. Like in the circular tumor case, all these ratio parameters vary in the range between 0 and 1 for the best searching performance.

Fig. 5 shows the evolution of the optimization parameters and the objective function in all the four injection cases. It is seen that all cases can converge within 300 generations, confirming the capacity of PSO in dealing with a large number of optimization parameters [25].

Table 4
Displacement parameters used in the elliptical tumor cases.

Strategy	k_{dh}	k_{dv}	k_{di}	k_β	d_{h0}	d_{v0}	d_{i0}	β_0
One-site	–	–	–	–	–	–	–	–
Two-site	✓	–	–	–	$1.25d_0$	–	–	–
Four-site	✓	✓	–	–	$1.25d_0$	$0.8d_0$	–	–
Eight-site	✓	✓	✓	✓	$1.25d_0$	$0.8d_0$	d_0	90°

However, if compared with the corresponding cases for the circular tumor, these cases generally require more generations to converge, reflecting the complexity of this geometrically irregular problem. Moreover, sudden jumps are observed after 100 or even 150 generations in the two-site and four-site injection cases, which were also reported in Tang et al. [25]. These sudden jumps may be attributed to the multi-extremum nature of the current optimization problem, which confirms the capability of the PSO in global optimum search.

Fig. 5 also reveals that the objective function J increases from 0.66 to 0.86 as the number of injection sites increases, which is also listed in Table 5. This confirms that the more injections, the better. The optimal temperature distribution for the four cases are presented in Fig. 6(a) ~ (d). It is not surprising to see that the one-site injection fails to meet the temperature requirements again. The circular temperature contour cannot fit the tumor's elliptical shape: On one hand overheating occurs at the tumor center and in the healthy tissue near the minor axis, and on the other hand underheating occurs inside the tumor along the major axis. This intrinsic mismatch can be mitigated by using the two-site injection strategy. As shown in Fig. 6(b), the two-site injection makes

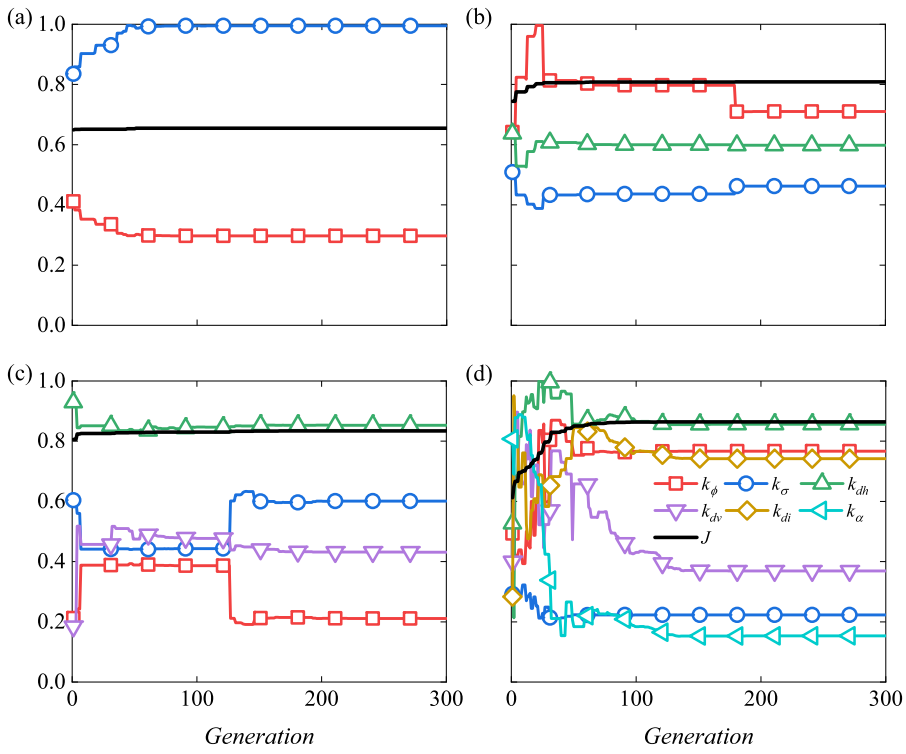

Fig. 5. PSO searching process for the cases on the elliptical tumor model: (a) one-site injection, (b) two-site injection, (c) four-site injection, and (d) eight-site injection.

Table 5
Optimization results for the one-, two-, four- and eight-site injection cases on the elliptical tumor model.

Strategy	R_{tum}	R_{tis}	R_{int}	R_{dose}	J	t_{opt}, min	V_{opt}, mm^2	$d_{h,opt}$, mm	$d_{v,opt}$, mm	$d_{i,opt}$, mm	β, °
One-site	0.620	0.996	0.516	0.335	0.66	19.8	0.367	–	–	–	–
Two-site	0.885	0.999	0.890	0.328	0.81	4.28	0.380	3.37	–	–	–
Four-site	0.974	0.999	0.884	0.327	0.83	7.23	0.381	4.80	1.55	–	–
Eight-site	1.000	1.000	0.995	0.327	0.86	0.99	0.381	4.82	1.33	3.34	13.8

the 43 °C line fit reasonably well with the tumor boundary and protects the healthy tissue from overheating, hence resulting in a significant increase in J. Unfortunately, it generates two small overheating spots inside the tumor.

The situation gets much improved if the number of injection sites are further increased to four. As shown in Fig. 6(c), the two injection sites added in the minor axis help remove the overheating spots, making the temperature at the tumor center the highest. However, it requires about 3 more minutes waiting time for the operation of AMF, and there are still some temperature mismatch around the tumor boundary, as also revealed in the plots in Fig. 6(e) and (f). This temperature mismatch can be further mitigated by adding four more sites in the eight-site injection case. The added four more sites help redistribute the MNPs, greatly reducing the waiting time to just about 1 min.

It is interesting to see from Table 5 that the optimal total MNP doses in all four cases fluctuate only marginally with less than 3% difference. They are also very close to the optimal total doses suggested for the circular tumor of the same area. This indicates that the MNP dose is neither sensitive to the injection strategy nor sensitive to the shape of tumor. Instead, it seems mainly dependent on the area of the tumor, consistent with observations in clinical trials [44].

In the eight-site injection case, the optimal inclination angle for four injection sites is found to be $\beta = 13.8°$. To check how sensitive the optimization is to this inclination angle, an additional eight-site injection case is considered, in which the inclination angle is fixed at $\beta = 30°$. As shown and compared in Fig. 7 as well as in Table 6, these two inclination angles lead to quite different results. The globally optimal injection sites in the $\beta = 13.8°$ case form an elliptical pattern alike to the shape of the tumor. On the contrary, the eight sites in the $\beta = 30°$ case form a figure "8" pattern, with the two sites in the major axis being further away and the two sites in the minor axis being much closer. The latter pattern results in a bit mismatch in temperature along the tumor boundary, leading to a slightly smaller J.

Another apparent difference between these two cases lies in the waiting time. The global optimal $\beta = 13.8°$ case only requires to wait for about 1 min, while the $\beta = 30°$ case requires to wait for a much longer time, i.e., about 8 min. This long waiting time allows the MNPs to sufficiently diffuse, as confirmed in Fig. 7(a), resulting in much smoother temperature distribution inside the tumor after the AMF is applied, as shown in Fig. 7(c).

3.3. Thermal dose

In the above optimization work, the ideal outcome is a temperature field in which the temperature in the tumor is between 43 °C and 46 °C, while the temperature in the surrounding healthy tissue stays below 43 °C. In practice, the amount of cell death in hyperthermia treatment depends not only on the temperature, but also on the time of exposure to heat, i.e., thermal dose [45]. In this section, we will check whether the optimal temperature distributions obtained for the two tumor models are still good if the exposure time is taken into account.

The cumulative-equivalent-minutes-at-43 °C (CEM43) model is a widely used model to evaluate thermal dose, which translates different temperature–time histories to a single value representing a "thermal isoeffect dose". Specifically, it is an equivalent exposure time expressed

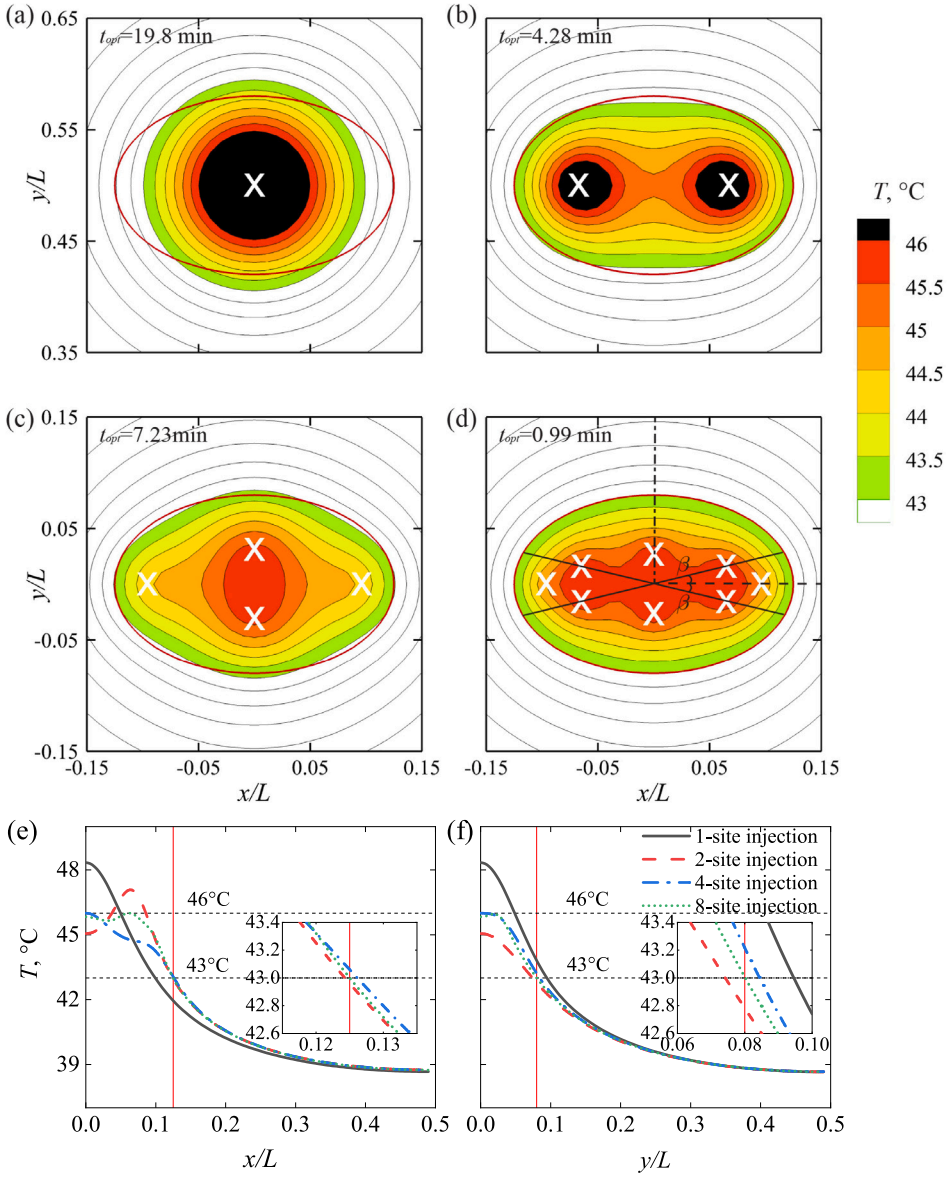

Fig. 6. (a)–(d) Optimal temperature distributions on the elliptical tumor model for the one-, two-, four- and eight-site injection cases, respectively. The white crosses denote the injection sites. The red ellipse represents tumor boundary. The black color denotes regions with temperature above 46 °C, the white color denotes regions with temperature under 43 °C, and the other colors denote regions with temperature ranging between 43 °C and 46 °C. (e) and (f) optimal temperature distribution along the x and y axes, respectively. The insets show more details near the tumor boundaries, i.e., $x/L = 0.125$ and $y/L = 0.8$ as represented by the vertical red lines.

Table 6
Comparison of optimization results between two eight-site injection cases with different inclination angles.

Inclination angle	R_{tum}	R_{tis}	R_{int}	R_{dose}	J	t_{opt}, min	V_{opt}, 10^{-7} m^2	$d_{h,opt}$, mm	$d_{v,opt}$, mm	$d_{i,opt}$, mm
$\beta = 30°$	1.000	1.000	0.940	0.322	0.85	8.03	3.89	5.62	0.49	3.50
$\beta = 13.8°$	1.000	1.000	0.995	0.327	0.86	0.99	3.81	4.82	1.33	3.34

as minutes at the reference temperature of 43 °C, i.e.,

$$\text{CEM43} = \sum_{i=1}^{l} C_{EM}{}^{43-T_i}\,\delta t \tag{12}$$

where T_i is the temperature in °C at the ith time step, δt represents the time interval, and l denotes the total number of time steps. C_{EM} is set as 0.5 when $T_i > 43$ °C and 0.25 otherwise [46]. It was suggested that when CEM43 reaches 60 min, the related cells are regarded as killed by the heat [19,45]. With this hypothesis, we assess the hyperthermia treatment efficacy through the ratio of killed cells in a tumor or in its surrounding healthy tissue

$$R_{CEM43} = \frac{S_{CEM43\geq 60\ \text{min}}}{S_{tum}} \tag{13}$$

With this definition, $R_{CEM43} = 1$ in tumor and 0 in healthy tissue correspond to the ideal hyperthermia treatment efficacy, i.e., all the tumor cells are killed while the healthy tissue stays safe.

By considering the effect of exposure time with the CEM43 model, the cell ablation in the tumor and healthy tissue is assessed for the two tumor models, starting from the optimal temperature distributions obtained in Sections 3.1 and 3.2. Note that, in this assessment the evolution of MNP diffusion, although much slower than thermal diffusion

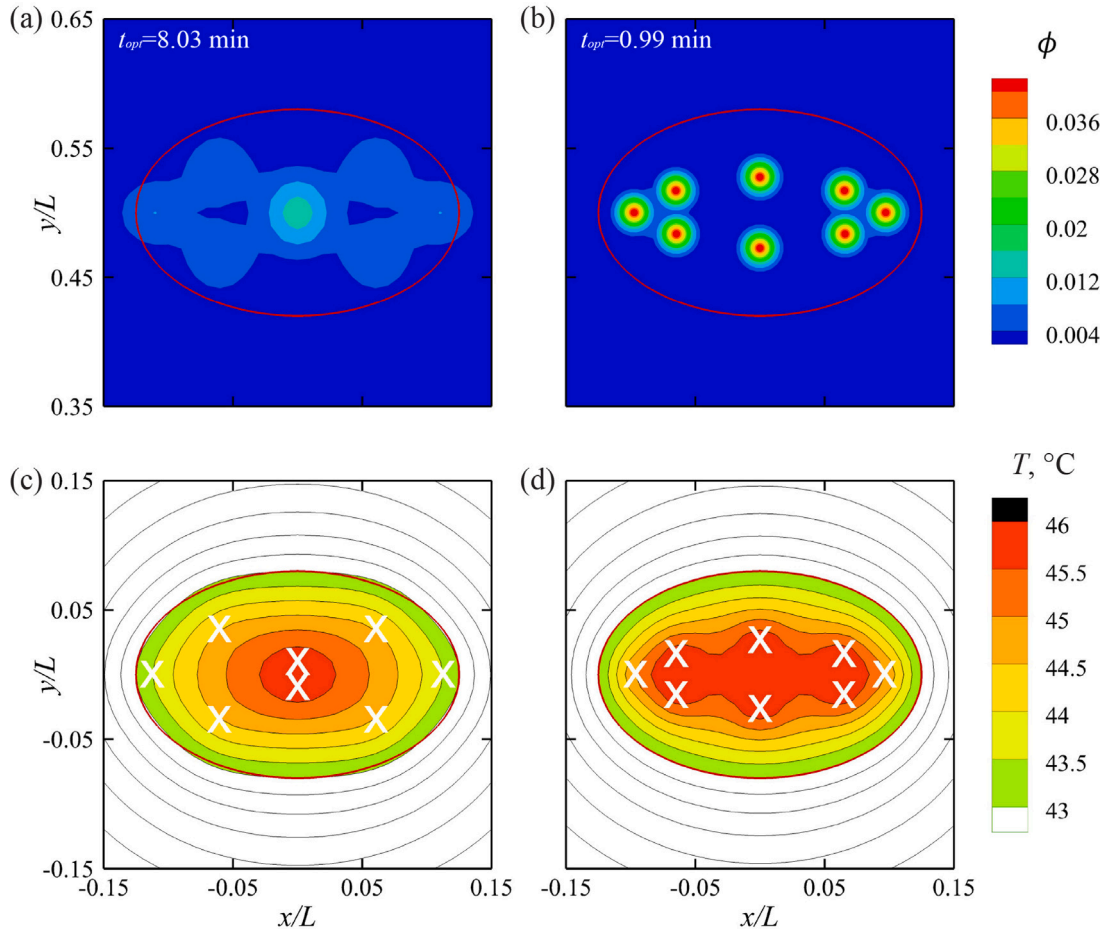

Fig. 7. Optimal concentration and temperature distributions in two different eight-site injection cases on the elliptical tumor model. In (a) and (c) four injection cites are arranged along the pre-determined $\beta = \pm 30°$ axes, whereas in (b) and (d) they are arranged along the $\beta = \pm 27.5°$ axes, which is the optimization result. The red ellipse represents tumor boundary. The white crosses denote the injection sites. In the temperature fields, the white color denotes regions with temperature under 43 °C, and the other colors denote regions with temperature ranging between 43 °C and 46 °C.

in the present study, is taken into account since the treatment time is usually long.

Fig. 8(a) presents the evolution of ablation ratios in the circular tumor model. It is not surprising to see that, for such an axisymmetric tumor model, ablation of cells in the surrounding healthy tissue starts to occur right at the instant when 100% ablation is achieved inside the tumor. Specifically, the one- and eight-site injection cases perfectly complete the tumor ablation (i.e., $R_{CEM43} = 1$ in tumor and 0 in healthy tissue) in 104.8 min and 126.6 min, respectively, at a similar level as in experimental observations [47]. The four-site injection case is a slight exception, which has $R_{CEM43} = 0.32\%$ healthy tissue destroyed when 100% ablation is achieved inside the tumor. This is caused by the slight mismatch of temperature requirement along the tumor-healthy-tissue interface at the start of ablation, as depicted in Fig. 3.

Although not presented here for brevity, it is also observed that in the one-site injection case an overheated (i.e., $T > 46$ °C) region appears at the tumor center at $t = 6.2$ min and, due to the MNP diffusion, disappears at $t = 38.0$ min. This 31.8 min overheat definitely influences the ablation efficacy [42]. As such, only the four- and eight-site injections can be considered to perform well for the circular tumor.

Different from the circular tumor, the elliptical tumor does not show any perfect treatment. As shown in Fig. 8(b) and listed in Table 7, in all the injection cases, not all tumor cells are killed when the healthy tissue starts to be destroyed. The one-site injection case performs the worst, in which only 67% tumor cells are killed and also overheat occurs from $t = 9.5$ to 26.2 min. Nevertheless, in the two- and eight-site injection cases no less than 90% tumor cells are ablated.

Table 7
R_{CEM43} in tumor and exposure time when healthy tissue begins to be injured.

Strategy	R_{CEM43} in tumor	Exposure time, min
One-site	0.67	60.7
Two-site	0.95	122.7
Four-site	0.83	101.5
Eight-site	0.90	104.3

The ablation process in the eight-site injection case is illustrated in Fig. 9. At the early stage (i.e., $t = 30$ min), the ablated area (the white ellipse) is thinner than the tumor due to the thinner pattern of the eight injection sites determined by the optimization of temperature requirements. As time advances, the MNPs diffuse almost uniformly in all directions. Consequently, the ablated area becomes thicker and gradually evolves towards a circle. At $t = 60$ min, it has almost the same but slightly smaller elliptic shape as the tumor. At $t = 120$ min, it reaches out of the tumor in the minor-axis direction, but is still inside in the major-axis direction. This asynchronism reflects that the almost perfect injection site pattern optimized through temperature requirements may not work perfectly if the exposure time is considered, especially for geometrically irregular tumor models.

4. Conclusions

In this study, the best MNP injection strategy for magnetic hyperthermia treatment was explored using a dedicated LBM modeling + PSO

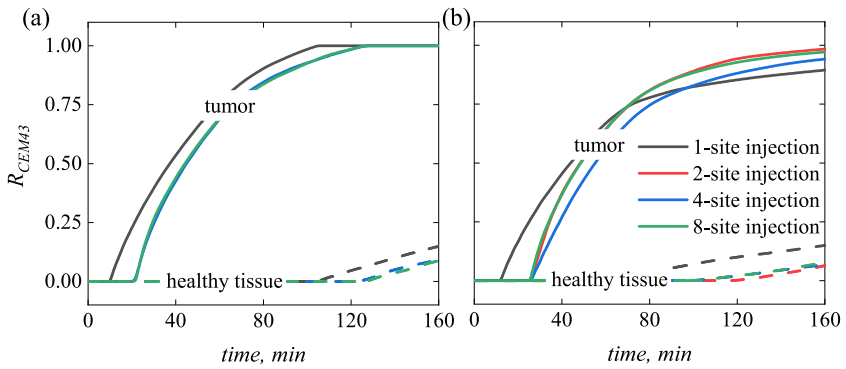

Fig. 8. Evolution of ablation ratio for (a) the circular tumor model and (b) the elliptical tumor model.

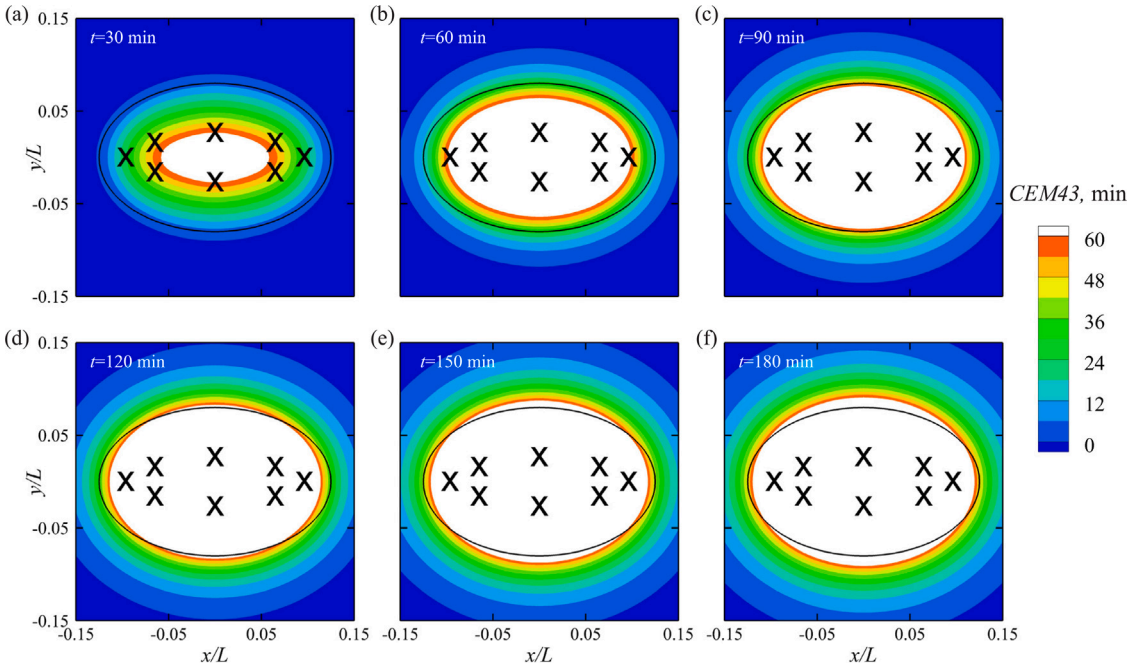

Fig. 9. Evolution of the ablation process in the eight-sight injection case for the elliptical tumor at (a) t = 30 min, R_{CEM43} = 0.15 in tumor and 0 in healthy tissue, (b) t = 60 min, R_{CEM43} = 0.64 in tumor and 0 in healthy tissue, (c) t = 90 min, R_{CEM43} = 0.85 in tumor and 0 in healthy tissue, (d) t = 120 min, R_{CEM43} = 0.93 in tumor and 0.02 in healthy tissue, (e) t = 150 min, R_{CEM43} = 0.97 in tumor and 0.07 in healthy tissue, (f) t = 180 min, R_{CEM43} = 0.98 in tumor and 0.11 in healthy tissue. The black crosses denote the injection sites determined by the optimization of temperature requirements. The black ellipse represents the tumor boundary and the white area represents the ablated region.

optimization framework. Two tumor models were considered, i.e., a circular model and an elliptical model that represent geometrically regular and irregular tumors, respectively. The results clearly indicated that the single-site injection strategy fails, even on the simplest circular tumor model. In this case, a significant portion of the tumor at the center overheats to more than 46 °C, causing serious inflammatory responses. On the contrary, the multi-site injection strategies generally work well for both regular and irregular tumor models in terms of temperature distribution. Multi-site injection can also significantly reduce the waiting time for MNP diffusion before the AMF operation. The more the injection sites, the better the performance. However, too many injection sites may cause inconvenience. Hence, four-site injection could be an appropriate strategy that balances the temperature requirements with practical complications.

The geometrical irregularity of the tumor requires more generations for the optimum search, since it needs more parameters to describe the injection strategy. However, the required MNP dose was found insensitive to the shape of tumor. It was also found that whether including the minimum MNP dose requirement (i.e., R_{dose}) or not in the objective function only slightly affects the optimization results by less than 2%. This implies that the minimum dose requirement has automatically been satisfied if the other three temperature requirements are satisfied.

If the thermal dose received by cells is considered, the optimal multi-site injection strategies perform generally well for both tumor models, especially for the circular tumor. For the elliptical tumor, if the optimal two- and eight-site injection strategies are adopted, no less than 90% tumor cells are killed when the healthy tissue starts to be ablated.

Although the simulation is only two dimensional and the optimization is conducted on very simplified tumor models, the framework adopted in this present study works well and is able to provide useful insights into magnetic hyperthermia treatment. In the near future, more realistic settings will be considered for magnetic hyperthermia simulations and optimizations, in which more physics are involved, such as the dynamics of perfusing flow in tissue, the buoyancy and Lorentz forces, and time-dependent diffusion of MNPs. Moreover, an improved optimization framework will be developed to take the heat exposure time into account.

CRediT authorship contribution statement

Qian Jiang: Conceptualization, Methodology , Investigation, Visualization, Formal analysis, Writing – original draft, Writing – review & editing. **Feng Ren:** Methodology, Investigation, Review & editing. **Chenglei Wang:** Methodology, Investigation, Review & editing. **Zhaokun Wang:** Investigation, Formal analysis, Review & editing. **Gholamreza Kefayati:** Conceptualization, Methodology, Review & editing. **Sasa Kenjeres:** Investigation, Review & editing. **Kambiz Vafai:** Investigation, Review & editing. **Yang Liu:** Methodology, Supervision, Review & editing. **Hui Tang:** Conceptualization, Methodology, Formal analysis, Investigation, Resources, Writing – review & editing, Supervision.

Declaration of competing interest

The authors declare the following financial interests/personal relationships which may be considered as potential competing interests: Hui Tang reports financial support was provided by the Research Grants Council of Hong Kong under General Research Fund.

Acknowledgments

This study was financially supported by the Research Grants Council of Hong Kong under General Research Fund (Project No. 15214418).

Appendix A. Evaluating Q in Eq. (1)

The last term Q in Eq. (1) represents the heat released from MNPs, induced by an external AMF with amplitude H_0 and frequency f. In general it includes the heat due to hysteresis loss and the heat from Neel and Brownian relaxation. According to Chang et al. [12], however, the size of MNPs used for magnetic hyperthermia is so small that the hysteresis loss can be neglected. Hence only the heat from the Neel and Brownian relaxation is considered, using the Rosensweig's model [48–50]

$$Q = \pi \mu_0 \chi_0 H_0^2 f \frac{2\pi f \tau_R}{1 + (2\pi f \tau_R)^2} \tag{A.1}$$

where μ_0 is the vacuum permeability. τ_R is the effective relaxation time and can be evaluated with the Neel relaxation time τ_N and the Brownian relaxation time τ_B as

$$\frac{1}{\tau_R} = \frac{1}{\tau_N} + \frac{1}{\tau_B} \tag{A.2}$$

where

$$\tau_N = \frac{\sqrt{\pi}}{2} \frac{\tau_0 \exp(\frac{KV_M}{k_B T})}{\sqrt{\frac{KV_M}{k_B T}}} \tag{A.3}$$

$$\tau_B = \frac{3\mu V_H}{k_B T} \tag{A.4}$$

Here τ_0 is a constant reference time, K is the anisotropy constant reflecting the level of directional dependence of the material's magnetic moment, k_B is the Boltzmann constant, and μ is the fluid viscosity. V_M and V_H are magnetic volume and hydrodynamic volume of the MNP, respectively, both equal to $\pi d_{mnp}^3/6$.

χ_0 in Eq. (A.1) accounts for equilibrium susceptibility and can be evaluated as [50]

$$\chi_0 = \chi_i \frac{3}{\xi} (\coth \xi - \frac{1}{\xi}) \tag{A.5}$$

where

$$\chi_i = \frac{\mu_0 \phi M_d^2 V_M}{3 k_B T} \tag{A.6}$$

$$\xi = \frac{\mu_0 M_d H_0 V_M}{k_B T} \tag{A.7}$$

Table A.1
Parameters for the Rosensweig's model [49].

Parameters	Value
Boltzmann constant, k_B (J/K)	1.38×10^{-23}
MNP mean diameter, d_{mnp} (m)	12×10^{-9}
Vacuum permeability, μ_0 (Tm/A)	$4\pi \times 10^{-7}$
Domain magnetization, M_d (A/m)	4.46×10^5
Anisotropy constant, K (J/m^3)	2.3×10^4
Viscosity of carrier fluid, μ (Pa-s)	6.92×10^{-4}
Magnetic field frequency, f (Hz)	2.0×10^5
Magnetic field amplitude, H_0 (A/m^2)	8×10^3
Magnetic attempt time, τ_0 (s)	1.0×10^{-9}

Here M_d is the domain magnetization. The properties for calculation of source term Q are listed as Table A.1. Note that temperature T appears in Eqs. (A.3), (A.4), (A.6) and (A.7), making the solution of Eq. (1) very challenging. To simplify the problem, in these equations T is fixed at a constant temperature 43 °C, which has also be adopted in other studies such as Refs. [49,51].

Appendix B. Solving PBHTE using LBM

The LBM is a relatively new CFD method for fluid flow and heat/mass transfer simulations. Unlike traditional CFD methods, which solve the conservation equations of macroscopic properties numerically, LBM models the fluid particles by distribution functions through consecutive streaming and collision processes over a number of square lattices [52–54]. Zhang [34] was probably the first to apply the LBM to solving PBHTE, successfully demonstrating the capability of LBM in simulating bioheat problems. This mesoscopic approach was then widely applied for bioheat studies [18,55,56]. In the present study, a D2Q5 (i.e., two-dimensional five-discrete-velocity) MRT (i.e., multiple-relaxation-time, a collision model that is used to improve the numerical stability [57]) LBM scheme is applied to obtain the temperature field by solving Eq. (1) [58]

$$\begin{aligned} \mathbf{g}(x_k + \delta_t \mathbf{e}, t_n + \delta_t) - \mathbf{g}(x_k, t_n) &= -\mathbf{N}^{-1} \mathbf{\Theta} [\mathbf{n} - \mathbf{n}^{(eq)}]|_{(x_k, t_n)} \\ &\quad + \mathbf{N}^{-1} \delta_t (\mathbf{I} - \mathbf{\Theta}/2) \mathbf{\Psi} \end{aligned} \tag{B.1}$$

where $\mathbf{g}(x_k, t_n) = (g_0(x_k, t_n), g_1(x_k, t_n), \ldots, g_4(x_k, t_n))^{\mathrm{T}}$ is a five-dimensional distribution function vector at time t_n and node x_k. $\mathbf{e}$ describes unit velocities along 5 discrete directions

$$e_i = \begin{cases} (0,0) & i = 0 \\ (\cos[(i-1)\pi/2], \sin[(i-1)\pi/2])c & i = 1 \sim 4 \end{cases} \tag{B.2}$$

where $c = \delta_x/\delta_t$ is the lattice speed, which is 1 since $\delta_x = \delta_t$ in the MRT model. $\mathbf{N}$ is a 5×5 orthogonal transformation matrix

$$\mathbf{N} = \begin{pmatrix} 1 & 1 & 1 & 1 & 1 \\ 0 & 1 & 0 & -1 & 0 \\ 0 & 0 & 1 & 0 & -1 \\ -4 & 1 & 1 & 1 & 1 \\ 0 & 1 & -1 & 1 & -1 \end{pmatrix} \tag{B.3}$$

$\mathbf{\Theta}$ is the diagonal relaxation matrix

$$\mathbf{\Theta} = \mathrm{diag}(1, 1/\tau_T, 1/\tau_T, 1.5, 1.5) \tag{B.4}$$

where τ_T can be linked to thermal diffusivity of nanofluid in Chapman–Enskog analysis on Eq. (1) as

$$\alpha_{nf} = c_{sT}^2 (\tau_T - 0.5) \delta_t \tag{B.5}$$

$\mathbf{n}$ and $\mathbf{n}^{(eq)}$ are the velocity moments and the corresponding equilibrium velocity moments, respectively. $\mathbf{\Psi}$ is a source vector including the heat induced by both blood perfusion and nanoparticles. More details about the D2Q5 MRT LBM can be found in [58].

In this study, the adiabatic boundary condition is applied at the four sides of the healthy tissue block, as depicted in Fig. 1. As such, the Neumann boundary condition proposed by Yoshino and Inamuro [59] is

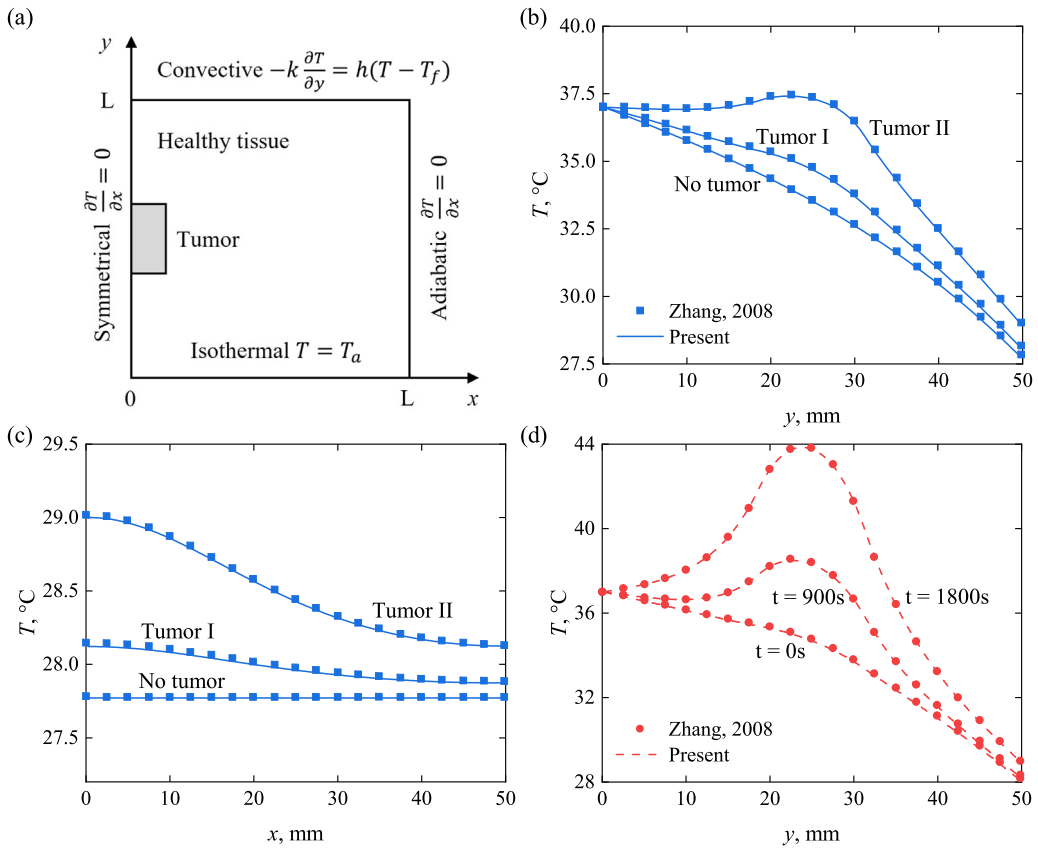

Fig. B.1. Validation of the current LBM based PBHTE solver with existing simulation results: (a) Schematic of the hyperthermia problem studied in Zhang [34]; Comparison of temperature distributions in the three steady heat transfer scenarios (b) along the y axis and (c) along the $y = L$ line; (d) Comparison of temperature distributions in a transient heat transfer process.

Table B.1
Studies on computational domain size and grid number.

Domain size	L/d_{tum}	T_c, °C	T_r, °C	Err_c, %	Err_r, %
	5	45.88	43.00	0.36	0.39
	10	45.71	42.83	–	–
Grid number	$N_x \times N_y$	T_c, °C	T_r, °C	Err_c, %	Err_r, %
	50 × 50	47.61	43.97	3.77	2.27
	100 × 100	45.88	43.00	0.03	0.05
	200 × 200	45.89	43.02	–	–

adopted, which enforces a zero normal heat flux at the four sides. At the tumor–healthy-tissue interface, the continuous temperature condition is enforced, i.e., $T_{tum} = T_{tis}$.

The influence of computational domain size and grid number is also assessed. Take the eight-site injection case on the circular tumor as an example, two sets of domain size and three sets of grids are considered, as listed in Table B.1. The simulated temperatures at two selected locations, i.e., the tumor center (T_c) and the rightmost point on the tumor–healthy-tissue interface (T_r), are compared, and the comparison results suggest that the domain size of $5d_{tum} \times 5d_{tum}$ and the grid number of 100 × 100 are sufficient for this study.

To validate our LBM solver, we simulate the same problem studied in Zhang [34], where, as sketched in Fig. B.1(a), a square tumor of $0.25L \times 0.25L$ is surrounded by the healthy tissue that is represented by a rectangle of $2L \times L$, where $L = 50$ mm. First, three steady heat transfer scenarios are simulated and compared with the results given in Zhang [34]: (1) No tumor—the tumor behaves exactly the same as the healthy tissue; (2) Tumor I—the tumor supplies 10 times the metabolic heat and blood perfusion in the healthy tissue; (3) Tumor II—the tumor supplies 100 times the metabolic heat and blood perfusion in the healthy tissue. The simulated temperature distributions along $x = 0$ and $y = L$ are presented in Fig. B.1(c) and (d), respectively. They agree very well with the reference. Then, a transient heat transfer process is simulated, in which the tumor generates heat with a constant rate. Good agreements are also achieved in Fig. B.1(b) between the simulated temperature profiles along $x = 0$ and the data from Zhang [34] at three selected instants. This proves the capability of our solver in solving transient heat transfer phenomena.

In another validation study, we simulated the temperature distribution in a rat limb that is subjected to magnetic hyperthermia treatment, and compared it with experimental data [17]. The distribution of injected ferrofluid is assumed to be a Gaussian shape. The reasonably good agreements under two different ferrofluid doses as shown in Fig. B.2 confirm the validity of using the present 2D framework to simulate simple 3D problems.

Appendix C. Particle swarm optimization

Particle swarm optimization (PSO) is a heuristic optimization algorithm, which performs stochastic search and does not rely on initial conditions, makes few or no assumptions about the problem being optimized and can search very large spaces of candidate solutions [43]. As a population-based iterative algorithm, PSO emulates the swarm behavior of insects, animals herding, birds flocking, and fish schooling where these swarms search for food in a collaborative manner, and each member searches by learning the experience from itself and others [60]. Each member in the swarm can be treated as a particle. The movements of these particles are guided by their own best-known position in the search-space as well as the entire swarm's best-known position. As such, three mechanisms are involved in the search: inertia, self recognition, and social communication, which enable PSO to balance

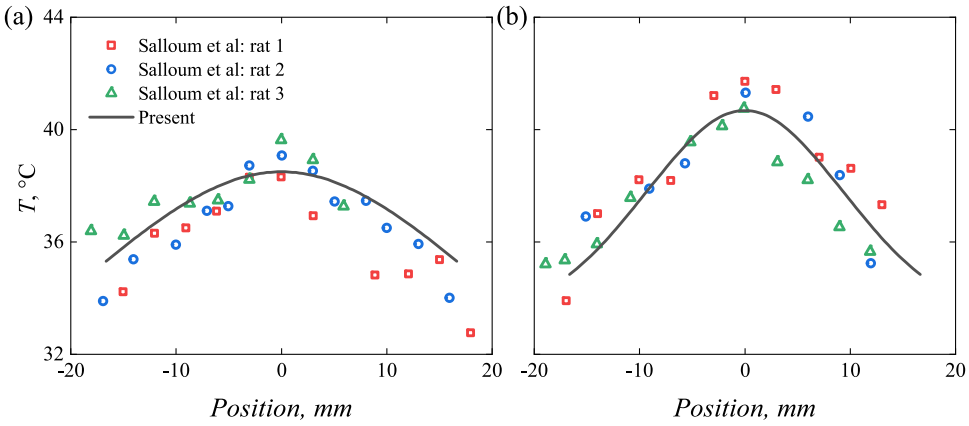

Fig. B.2. Validation of the current LBM based PBHTE solver with existing experimental data obtained from rat limbs [17]: (a) 0.1 cc and (b) 0.2 cc ferrofluid injection.

Table C.1
Validation of the current PSO algorithm with benchmark optimization problems.

Function	Type	Dimension	Numerical minimum	Theoretical minimum
Sphere function	Unimodal	5	7.8451×10^{-8}	0
Shubert function	Multimodal	2	-1.8673×10^{2}	-1.8673×10^{2}
Rastrigin function	Multimodal	2	0	0
Rastrigin function	Multimodal	5	3.3657×10^{-5}	0

local exploitation and global exploration [61]. Since it is easy to implement and capable of dealing with complex multimodal problems, after being introduced in 1995 by Kennedy and Eberhart [43], PSO has been successfully demonstrated in various applications [62–65], and evolved into many improved schemes [60,66–71].

In the present study, the PSO with linear decreasing inertia weight is adopted

$$v^{t+1} = wv^t + c_1 r_1 (p^t - x^t) + c_2 r_2 (g^t - x^t) \tag{C.1}$$

$$x^{t+1} = v^t + x^t \tag{C.2}$$

where x denotes the position of particles and v denotes their velocity. w is the inertia weight. c_1 and c_2 are the acceleration constants describing the rate of stochastic accelerations that pull the particles toward their own and the group's best positions. In this study, w linearly reduces from 0.8 to 0 (from 0.9 to 0.4 in the cases not considering R_{dose}), while c_1 and c_2 are set as 1.5. r_1 and r_2 are random variables in the range of $[0, 1]$. p and g are the historical best positions of the current particle and the whole group, respectively.

To validate our PSO model, we perform optimization on three representative benchmark functions as follows [72,73]

Sphere Function:

$$f(x) = \sum_{i=1}^{n} x_i^2$$

Shubert Function:

$$f(x) = \sum_{i=1}^{n} i \cos((i+1)x_1 + 1) \sum_{i=1}^{n} i \cos((i+1)x_2 + 1)$$

Rastrigin Function:

$$f(x) = 10n + \sum_{i=1}^{n} (x_i^2 - 10\cos(2\pi x_i))$$

The sphere function is unimodal, while the Shubert and Rastrigin functions are multimodal with a large number of local extremes. The optimization results are compared with theoretical maximums as listed in Table C.1. The good performance of our PSO model ensure its validity in dealing with the optimization problem in the present study.

References

[1] Sharma S, Shrivastava N, Rossi F, Thanh NTK, et al. Nanoparticles-based magnetic and photo induced hyperthermia for cancer treatment. Nano Today 2019;29:100795.

[2] Vilas-Boas V, Carvalho F, Espiña B. Magnetic hyperthermia for cancer treatment: Main parameters affecting the outcome of in vitro and in vivo studies. Molecules 2020;25(12):2874.

[3] Jose J, Kumar R, Harilal S, Mathew GE, Parambi DGT, Prabhu A, et al. Magnetic nanoparticles for hyperthermia in cancer treatment: An emerging tool. Environ Sci Pollut Res 2020;27(16):19214–25.

[4] Ma J, Yang X, Sun Y, Yang J. Theoretical investigation on the thermo-mechanical responses of the human skin during thermal therapy. Int J Mech Sci 2019;161:105041.

[5] Lin C-T, Liu K-C. Estimation for the heating effect of magnetic nanoparticles in perfused tissues. Int Commun Heat Mass Transfer 2009;36(3):241–4.

[6] Giordano MA, Gutierrez G, Rinaldi C. Fundamental solutions to the bioheat equation and their application to magnetic fluid hyperthermia. Int J Hyperth 2010;26(5):475–84.

[7] Yang C-y. Determining the heat strength required in hyperthermia treatments. Int Commun Heat Mass Transfer 2014;57:282–5.

[8] Das P, Colombo M, Prosperi D. Recent advances in magnetic fluid hyperthermia for cancer therapy. Colloids Surfaces B 2019;174:42–55.

[9] Kumar CSSR, Mohammad F. Magnetic nanomaterials for hyperthermia-based therapy and controlled drug delivery. Adv Drug Deliv Rev 2011;63(9):789–808.

[10] Laurent S, Dutz S, Häfeli UO, Mahmoudi M. Magnetic fluid hyperthermia: Focus on superparamagnetic iron oxide nanoparticles. Adv Colloid Interface Sci 2011;166(1–2):8–23.

[11] Karponis D, Azzawi M, Seifalian A. An arsenal of magnetic nanoparticles; perspectives in the treatment of cancer. Nanomedicine 2016;11(16):2215–32.

[12] Chang D, Lim M, Goos JA, Qiao R, Ng YY, Mansfeld FM, et al. Biologically targeted magnetic hyperthermia: Potential and limitations. Front Pharmacol 2018;9:831.

[13] Kosari E, Vafai K. Transport and dynamic analysis of magnetic nanoparticles in brain microvascular vessels. Phys Fluids 2021;33(8):081907.

[14] Ahamed M, Alhadlaq HA, Alam J, Khan M, Ali D, Alarafi S. Iron oxide nanoparticle-induced oxidative stress and genotoxicity in human skin epithelial and lung epithelial cell lines. Curr Pharm Des 2013;19(37):6681–90.

[15] Liangruksa M, Ganguly R, Puri IK. Parametric investigation of heating due to magnetic fluid hyperthermia in a tumor with blood perfusion. J Magn Magn Mater 2011;323(6):708–16.

[16] Salloum M, Ma RH, Weeks D, Zhu L. Controlling nanoparticle delivery in magnetic nanoparticle hyperthermia for cancer treatment: Experimental study in agarose gel. Int J Hyperth 2008;24(4):337–45.

[17] Salloum M, Ma R, Zhu L. An in-vivo experimental study of temperature elevations in animal tissue during magnetic nanoparticle hyperthermia. Int J Hyperth 2008;24(7):589–601.

[18] Golneshan AA, Lahonian M. Diffusion of magnetic nanoparticles in a multi-site injection process within a biological tissue during magnetic fluid hyperthermia using lattice Boltzmann method. Mech Res Commun 2011;38(6):425–30.

[19] Singh G, Kumar N, Avti PK. Computational evaluation of effectiveness for intra-tumoral injection strategies in magnetic nanoparticle assisted thermotherapy. Int J Heat Mass Transfer 2020;148:119129.

[20] Tang Y-d, Jin T, Flesch RCC. Impact of different infusion rates on mass diffusion and treatment temperature field during magnetic hyperthermia. Int J Heat Mass Transfer 2018;124:639–45.

[21] Salloum M, Ma R, Zhu L. Enhancement in treatment planning for magnetic nanoparticle hyperthermia: Optimization of the heat absorption pattern. Int J Hyperth 2009;25(4):309–21.

[22] Tang Y, Su H, Flesch RCC, Jin T. An optimization method for magnetic hyperthermia considering nelder-mead algorithm. J Magn Magn Mater 2022;545:168730.

[23] Di Barba P, Dughiero F, Sieni E. Synthesizing distributions of magnetic nanoparticles for clinical hyperthermia. IEEE Trans Magn 2012;48(2):263–6.

[24] Venter G. Review of optimization techniques, in books: Mechanical and mechatronic engineering. Wiley Online Library; 2010.

[25] Tang Y-D, Jin T, Flesch RC, Jiang H-Y. Simultaneous optimization of injection dose and location for magnetic hyperthermia using metaheuristic algorithms. IEEE Trans Magn 2019;56(1):1–6.

[26] Di Barba P, Dughiero F, Sieni E. Field synthesis for the optimal treatment planning in magnetic fluid hyperthermia. Arch Electr Eng 2012;57–67.

[27] Pennes HH. Analysis of tissue and arterial blood temperatures in the resting human forearm. J Appl Physiol 1948;1(2):93–122.

[28] Attar MM, Haghpanahi M, Amanpour S, Mohaqeq M. Analysis of bioheat transfer equation for hyperthermia cancer treatment. J Mech Sci Technol 2014;28(2):763–71.

[29] Mahmoudi K, Bouras A, Bozec D, Ivkov R, Hadjipanayis C. Magnetic hyperthermia therapy for the treatment of glioblastoma: A review of the therapy's history, efficacy and application in humans. Int J Hyperth 2018;34(8):1316–28.

[30] Rodrigues HF, Capistrano G, Bakuzis AF. In vivo magnetic nanoparticle hyperthermia: A review on preclinical studies, low-field nano-heaters, noninvasive thermometry and computer simulations for treatment planning. Int J Hyperth 2020;37(3):76–99.

[31] Buongiorno J. Convective transport in nanofluids. J Heat Transfer 2006.

[32] Ghasemi B, Aminossadati SM, Raisi A. Magnetic field effect on natural convection in a nanofluid-filled square enclosure. Int J Therm Sci 2011;50(9):1748–56.

[33] Sundar LS, Singh MK, Sousa ACM. Investigation of thermal conductivity and viscosity of Fe_3O_4 nanofluid for heat transfer applications. Int Commun Heat Mass Transfer 2013;44:7–14.

[34] Zhang H. Lattice Boltzmann method for solving the bioheat equation. Phys Med Biol 2008;53(3):N15.

[35] AlAmiri A, Khanafer K, Vafai K. Fluid-structure interactions in a tissue during hyperthermia. Numer Heat Transfer A 2014;66(1):1–16.

[36] Tang Y-d, Jin T, Flesch RCC. Effect of mass transfer and diffusion of nanofluid on the thermal ablation of malignant cells during magnetic hyperthermia. Appl Math Model 2020;83:122–35.

[37] Gibanov NS, Sheremet MA, Oztop HF, Nusier OK. Convective heat transfer of ferrofluid in a lid-driven cavity with a heat-conducting solid backward step under the effect of a variable magnetic field. Numer Heat Transfer A 2017;72(1):54–67.

[38] Hajmohammadi M, Gholamrezaie S, Ahmadpour A, Mansoori Z. Effects of applying uniform and non-uniform external magnetic fields on the optimal design of microchannel heat sinks. Int J Mech Sci 2020;186:105886.

[39] Lang J, Erdmann B, Seebass M. Impact of nonlinear heat transfer on temperature control in regional hyperthermia. IEEE Trans Biomed Eng 1999;46(9):1129–38.

[40] Kosari E, Vafai K. Thermal tissue damage analysis for magnetothermal neuromodulation and lesion size minimization. Brain Multiphysics 2020;1:100014.

[41] Chen S, Doolen GD. Lattice Boltzmann method for fluid flows. Annu Rev Fluid Mech 1998;30(1):329–64.

[42] Hervault A, Thanh NTK. Magnetic nanoparticle-based therapeutic agents for thermo-chemotherapy treatment of cancer. Nanoscale 2014;6(20):11553–73.

[43] Kennedy J, Eberhart R. Particle swarm optimization. In: Proceedings of ICNN'95-International conference on neural networks, Vol. 4. IEEE; 1995, p. 1942–8.

[44] Maier-Hauff K, Ulrich F, Nestler D, Niehoff H, Wust P, Thiesen B, et al. Efficacy and safety of intratumoral thermotherapy using magnetic iron-oxide nanoparticles combined with external beam radiotherapy on patients with recurrent glioblastoma multiforme. J Neurooncol 2011;103(2):317–24.

[45] Dewhirst MW, Viglianti B, Lora-Michiels M, Hanson M, Hoopes P. Basic principles of thermal dosimetry and thermal thresholds for tissue damage from hyperthermia. Int J Hyperth 2003;19(3):267–94.

[46] Kandala SK, Liapi E, Whitcomb LL, Attaluri A, Ivkov R. Temperature-controlled power modulation compensates for heterogeneous nanoparticle distributions: A computational optimization analysis for magnetic hyperthermia. Int J Hyperth 2018.

[47] Dewey WC, Hopwood LE, Sapareto SA, Gerweck LE. Cellular responses to combinations of hyperthermia and radiation. Radiology 1977;123(2):463–74.

[48] Zhang C, Johnson DT, Brazel CS. Numerical study on the multi-region bio-heat equation to model magnetic fluid hyperthermia (MFH) using low curie temperature nanoparticles. IEEE Trans NanoBioscience 2008;7(4):267–75.

[49] Purushotham S, Ramanujan RV. Modeling the performance of magnetic nanoparticles in multimodal cancer therapy. J Appl Phys 2010;107(11):114701.

[50] Rosensweig RE. Heating magnetic fluid with alternating magnetic field. J Magn Magn Mater 2002;252:370–4.

[51] Maenosono S, Saita S. Theoretical assessment of FePt nanoparticles as heating elements for magnetic hyperthermia. IEEE Trans Magn 2006;42(6):1638–42.

[52] Wang Z, Wang C, Zhao F, Qi N, Lockington D, Ramaesh K, et al. Simulation of fluid-structure interaction during the phaco-emulsification stage of cataract surgery. Int J Mech Sci 2022;214:106931.

[53] Ren F, Wang C, Tang H. Active control of vortex-induced vibration of a circular cylinder using machine learning. Phys Fluids 2019;31:093601.

[54] Wang C, Tang H, Duan F, Simon CM. Control of wakes and vortex-induced vibrations of a single circular cylinder using synthetic jets. J Fluids Struct 2016;60:160–79.

[55] Das K, Mishra SC. Estimation of tumor characteristics in a breast tissue with known skin surface temperature. J Therm Biol 2013;38(6):311–7.

[56] Das K, Singh R, Mishra SC. Numerical analysis for determination of the presence of a tumor and estimation of its size and location in a tissue. J Therm Biol 2013;38(1):32–40.

[57] Lallemand P, Luo L-S. Theory of the lattice Boltzmann method: Dispersion, dissipation, isotropy, Galilean invariance, and stability. Phys Rev E 2000;61(6):6546.

[58] Liu Q, He Y-L, Li Q, Tao W-Q. A multiple-relaxation-time lattice Boltzmann model for convection heat transfer in porous media. Int J Heat Mass Transfer 2014;73:761–75.

[59] Yoshino M, Inamuro T. Lattice Boltzmann simulations for flow and heat/mass transfer problems in a three-dimensional porous structure. Internat J Numer Methods Fluids 2003;43:183–98.

[60] Liang JJ, Qin AK, Suganthan PN, Baskar S. Comprehensive learning particle swarm optimizer for global optimization of multimodal functions. IEEE Trans Evol Comput 2006;10(3):281–95.

[61] He G, Huang N-j. A modified particle swarm optimization algorithm with applications. Appl Math Comput 2012;219(3):1053–60.

[62] Wang Y, Zhao W, Zhou G, Wang C. Analysis and parametric optimization of a novel sandwich panel with double-V auxetic structure core under air blast loading. Int J Mech Sci 2018;142:245–54.

[63] Xu J, Chen Y, Tai Y, Xu X, Shi G, Chen N. Vibration analysis of complex fractional viscoelastic beam structures by the wave method. Int J Mech Sci 2020;167:105204.

[64] Ye C, Yang J, Zhao H, Ding H. Task-dependent workpiece placement optimization for minimizing contour errors induced by the low posture-dependent stiffness of robotic milling. Int J Mech Sci 2021;205:106601.

[65] Ding X, Tong Z, Liu Y, Liu S. Dynamic axial crush analysis and design optimization of a square multi-cell thin-walled tube with lateral variable thickness. Int J Mech Sci 2018;140:13–26.

[66] Shi Y, Eberhart R. A modified particle swarm optimizer. In: 1998 IEEE international conference on evolutionary computation proceedings. IEEE world congress on computational intelligence (Cat. No. 98TH8360). IEEE; 1998, p. 69–73.

[67] Shi Y, Eberhart RC. Empirical study of particle swarm optimization. In: Proceedings of the 1999 congress on evolutionary computation-CEC99 (Cat. No. 99TH8406), Vol. 3. IEEE; 1999, p. 1945–50.

[68] Zhan Z-H, Zhang J, Li Y, Chung HS-H. Adaptive particle swarm optimization. IEEE Trans Syst Man Cybern B 2009;39(6):1362–81.

[69] Cao Y, Zhang H, Li W, Zhou M, Zhang Y, Chaovalitwongse WA. Comprehensive learning particle swarm optimization algorithm with local search for multimodal functions. IEEE Trans Evol Comput 2018;23(4):718–31.

[70] Minh H-L, Khatir S, Wahab MA, Cuong-Le T. An enhancing particle swarm optimization algorithm (EHVPSO) for damage identification in 3D transmission tower. Eng Struct 2021;242:112412.

[71] Gholami M, Fathi A, Baghestani AM. Multi-objective optimal structural design of composite superstructure using a novel MONMPSO algorithm. Int J Mech Sci 2021;193:106149.

[72] Oliva D, Esquivel-Torres S, Hinojosa S, Pérez-Cisneros M, Osuna-Enciso V, Ortega-Sánchez N, et al. Opposition-based moth swarm algorithm. Expert Syst Appl 2021;184:115481.

[73] Zaman HRR, Gharehchopogh FS. An improved particle swarm optimization with backtracking search optimization algorithm for solving continuous optimization problems. Eng Comput 2021;1–35.